

Internal variability in a 1000-yr control simulation with the coupled climate model ECHO-G – II. El Niño Southern Oscillation and North Atlantic Oscillation

By SEUNG-KI MIN^{1*}, STEPHANIE LEGUTKE², ANDREAS HENSE¹ and WON-TAE KWON³, ¹Meteorological Institute, University of Bonn, Auf dem Hügel 20, 53115 Bonn, Germany; ²Max Planck Institute for Meteorology, Bundesstrasse 53, 20146 Hamburg, Germany; ³Meteorological Research Institute, 460-18 Sindaebang-dong, Dongjak-gu, Seoul 156-720, Korea

(Manuscript received 30 July 2004; in final form 21 December 2004)

ABSTRACT

A 1000-yr control simulation (CTL) performed with the atmosphere–ocean global climate model ECHO-G is analysed with regard to the El Niño Southern Oscillation (ENSO) and North Atlantic Oscillation (NAO), the two major natural climatic variabilities, in comparison with observations and other model simulations. The ENSO-related sea surface temperature climate and its seasonal cycle in the tropical Pacific and a single Intertropical Convergence Zone in the eastern tropical Pacific are simulated reasonably, and the ENSO phase-locking to the annual cycle and the subsurface ocean behaviour related to equatorial wave dynamics are also reproduced well. The simulated amplitude of the ENSO signal is however too large and its occurrence is too regular and frequent. Also, the observed westward propagation of zonal wind stress over the equatorial Pacific is not captured by the model. Nevertheless, the ENSO-related teleconnection patterns of near-surface temperature (T2m), precipitation (PCP) and mean sea level pressure (MSLP) are reproduced realistically.

The NAO index, defined as the MSLP difference between Gibraltar and Iceland, has a ‘white’ noise spectrum similar to that of the detrended index obtained from observed data. The correlation and regression patterns of T2m, PCP and MSLP with the NAO index are also successfully simulated. However, the model overestimates the warming over the North Pacific in the high index phase of the NAO, a feature it shares with other coupled models. This might be associated with an enhanced Atlantic–Pacific teleconnection, which is hardly seen in the observations. A detection analysis of the NAO index shows that the observed recent 40–60 yr trend cannot be explained by the model’s internal variability while the recent 20–30 yr trend occurs with a more than 1% chance in ECHO-G CTL.

1. Introduction

In a companion paper (Min et al., 2005, hereafter Paper I), we have evaluated the internal variability of near-surface temperature (T2m), precipitation (PCP), and mean sea level pressure (MSLP) in a 1000-yr control simulation (CTL) with the ECHO-G coupled climate model and we have shown that ECHO-G is capable of reproducing well overall observed internal variability of the three surface variables. However, it is necessary to see whether the simulated internal variability on the interannual and decadal time-scales is well characterized by dominant natural climate variabilities such as the El Niño Southern Oscillation (ENSO) and North Atlantic Oscillation (NAO), as in the observations. For example, ECHO-G exhibited a strong spectral peak

centred near 2 yr in the global mean T2m, whereas observations show a broad band of strong energy on 3–9 yr time-scales (see fig. 3 of Paper I). This appears to occur related to too regular and frequent ENSO behaviours in the model.

The Intergovernmental Panel on Climate Change (IPCC) provides future climate change projections mainly using scenario simulations with atmosphere–ocean coupled general circulation models (AOGCMs; IPCC, 2001). However, the interpretation and reliability on the projection results should depend on the model skill in simulating the observed natural climate variability (e.g. Allen et al., 2000; Stott and Kettleborough, 2002), and the possible change of the ENSO and NAO in the future should be also addressed on the basis of such skills. At present, AOGCMs produce a very diverse response (large uncertainty) to the same external forcing or scenario, and predictions are likely to be very model-dependent in some phenomena (IPCC, 2001). In this context, the overall performance of many AOGCMs has been

*Corresponding author.
e-mail: skmin@uni-bonn.de

Table 1. Observational data for each analysed variable

Variable (abbreviation, unit)	Source	Resolution (latitude × longitude)	Analysis period (yr)	References
Near-surface temperature (T2m, °C)	HadCRUT2	5° × 5°	1856–2001	Jones and Moberg (2003) Rayner et al. (2003)
Sea surface temperature (SST, °C)	GISST2.2	1° × 1°	1903–1994	Rayner et al. (1996)
Precipitation (PCP, mm d ⁻¹)	CMAP CRU-PCP	2.5° × 2.5° 5° × 5°	1979–1999 1900–1998	Xie and Arkin (1997) Hulme (1992)
Mean sea level pressure (MSLP, hPa)	NCEP/NCAR reanalysis	2.5° × 2.5°	1958–2001	Kistler et al. (2001)
Zonal wind stress (none, N m ⁻²)	SOC	1° × 1°	Climate (1980–1993)	Josey et al. (1999)
Thermocline depth (Z20, m)	SIO	2° × 5°	1955–2000	White et al. (1999) Rodgers et al. (2004)
NAO index for DJFM (none, hPa)	CRU	–	1823/24–1999/2000	Jones et al. (1997)
NINO3 index (none, °C)	GISST2.2	–	1903–1994	–
SOI for DJF	CRU	–	1866–2003	Ropelewski and Jones (1987)

investigated by international cooperation, e.g. the Coupled Model Intercomparison Project (CMIP) and the Climate Variability and Predictability Project (CLIVAR).

Some recent studies from these efforts (Latif et al., 2001; AchutaRao and Sperber, 2002; Davey et al., 2002), where the skill of AOGCMs was evaluated and intercompared on the ENSO simulation, indicate that there have been improvements from the earlier stage, but still common or model-dependent problems exist in simulating ENSO-related features, e.g. sea surface temperature (SST) in the equatorial Pacific and ENSO teleconnections. There have been only a few studies of validating the NAO simulated by different AOGCM control runs. Stephenson and Pavan (2003) investigated the NAO response patterns from 17 AOGCM CTLs using the leading principal components (PCs) of wintertime surface temperatures as NAO indices. They showed that 13 out of the 17 models are able to capture the NAO response pattern of temperature, but several models show common problems of simulating overestimated teleconnection between the ENSO and the NAO.

The ECHO-G model has not yet participated in the model intercomparison studies particularly on ENSO and NAO simulations except for CMIP2+. Latif et al. (2001) analysed ECHO-2 (Frey et al., 1997; Venzke et al., 2000), an ancestor model of ECHO-G. In order to contribute to the assessment of the overall skill of AOGCMs, the objective of this paper is to evaluate ECHO-G on the simulation of the ENSO and NAO by comparing ECHO-G performance with those of observations and other AOGCMs analysed in CMIP1 (AchutaRao and Sperber, 2002; Stephenson and Pavan, 2003) and CLIVAR (Latif et al., 2001; Davey et al., 2002). In order to evaluate the ENSO simulation, the amplitude and frequency of the ENSO, the climatol-

ogy including the seasonal cycle and interannual variability of the tropical Pacific SST, the zonal wind stress and Intertropical Convergence Zone (ITCZ) in the equatorial Pacific, the ENSO phase-locking to annual cycle, the ocean subsurface behaviour and the ENSO responses of atmospheric variables (T2m, PCP and MSLP) are examined. For NAO validation, the MSLP variability in the Northern Hemisphere (NH), the spectral power and trend of the NAO index and NAO-related patterns of the atmospheric variables are analysed. The 1000 yr of ECHO-G CTL are divided into subsections with the same length as the observational period in some analyses.

Because the ECHO-G model and control experiments are described in detail in Paper I, we do not repeat them here. The observational data for model validation are described in Section 2. The model simulations of the ENSO and NAO are evaluated in Sections 3 and 4, respectively. A discussion and a conclusion are given in the final section.

2. Observational data

Table 1 shows the observational data used in this study with key references. For the evaluation of the model on the ENSO simulation, we use the Global Sea Ice and Sea Surface Temperature version 2.2 (GISST2.2) data set for the period of 1903–1994, the zonal wind stress data obtained from the Southampton Oceanography Centre (SOC), the thermocline depth estimated from the upper ocean temperature data set of the Scripps Institution of Oceanography (SIO), the NINO3 index defined as the spatial mean SST anomaly in the NINO3 region evaluated from GISST2.2, and the Southern Oscillation Index (SOI) from the Climate Research Unit (CRU) defined as the normalized

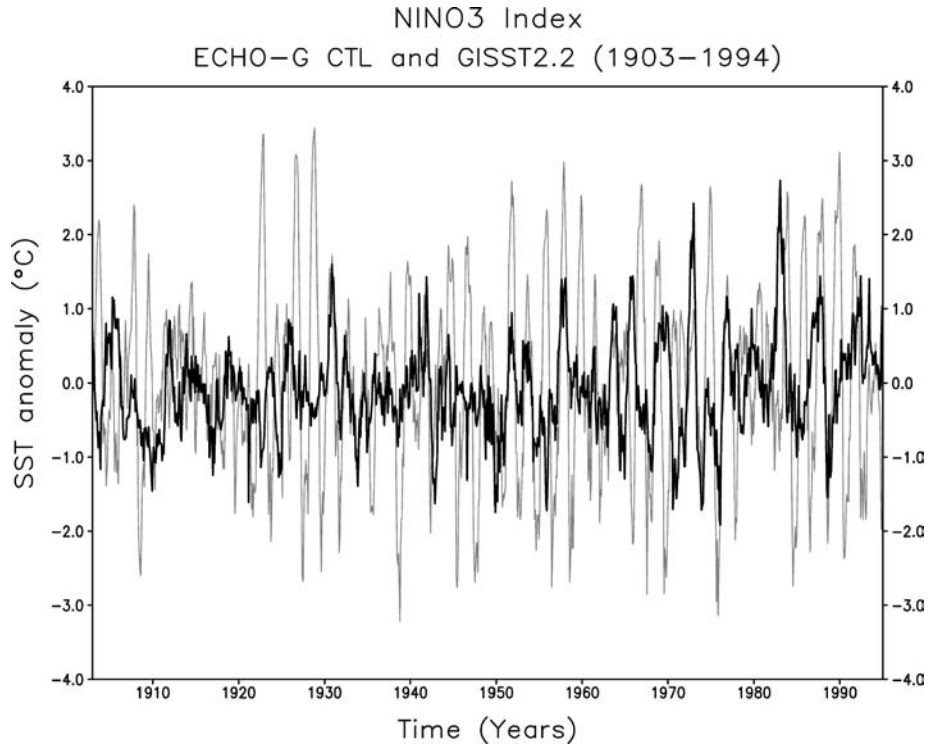


Fig. 1. Time series of the monthly NINO3 index from ECHO-G CTL (thin line) and GISST2.2 (thick line) from 1903 to 1994. The first 92 yr of the 1000-yr ECHO-G CTL are plotted.

pressure difference between Tahiti and Darwin (Ropelewski and Jones, 1987). For NAO analysis, we use a non-normalized index defined as the difference of December–March (DJFM) mean MSLPs between Gibraltar and South-west Iceland (Jones et al., 1997). To obtain the observed response patterns to the ENSO and NAO, the CRU T2m (HadCRUT2), two PCPs of the CRU and the Climate Prediction Center (CPC) Merged Analysis Precipitation (CMAP) and the MSLP from the National Centers for Environmental Prediction/National Center for Atmospheric Research (NCEP/NCAR) reanalysis are analysed.

3. El Niño Southern oscillation

3.1. ENSO amplitude and frequency

Figure 1 shows the monthly time series of the NINO3 index calculated from the GISST2.2 observations (1903–1994) and the first 92 yr of ECHO-G CTL. The NINO3 index is defined as the area-mean SST anomaly in the NINO3 domain (150–90°W and 5°S–5°N). The SST anomalies are evaluated relative to the 1961–1990 monthly means for the observations and to the whole 1000-yr monthly means for the model. The amplitudes of the NINO3 index in the model are larger than those observed. The standard deviation (STD) of the linearly detrended NINO3 index is 0.64°C for the observations (1905–1994) and 1.15°C for the model ranging from 0.93 to 1.23°C for 11 90-yr subsections of the 1000-yr simulation period.

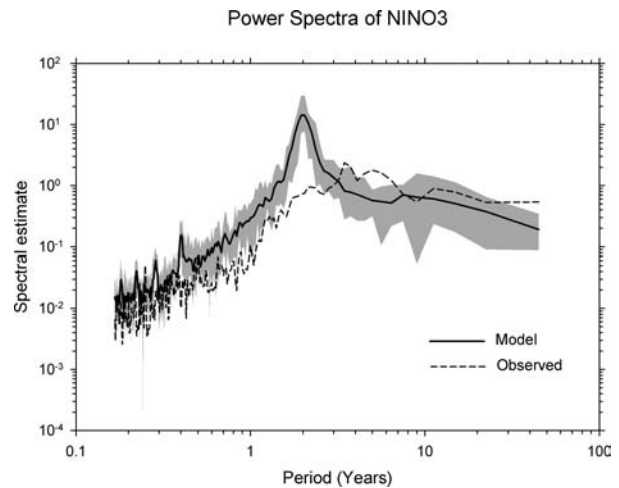


Fig. 2. Power spectra of the NINO3 index from ECHO-G CTL (solid line) and the observed NINO3 index (GISST2.2, 1905–1994). The shading indicates the maximum and minimum spectra from 11 90-yr sections of ECHO-G CTL and the solid line is the average of the 11 spectra.

The second feature of the simulated ENSO in the time series of Fig. 1 is that large positive/negative anomaly events (El Niño/La Niña) develop more frequently in the model than in the observations. This too frequent ENSO phenomenon in the model can be more clearly seen in the power spectrum analysis shown in Fig. 2. As for the global mean T2m (see fig. 3 of Paper I), the spectrum

of the NINO3 index in the model is calculated by averaging 11 spectra of the NINO3 index from 90-yr subsections of the 1000-yr CTL, while the observed spectrum is obtained from the 90-yr period of 1905–1994. The mean and range (maximum and minimum) of the model spectrum are depicted as a thick line and shading, respectively. The model spectrum of the NINO3 index exhibits a dominant 2-yr peak while the observational NINO3 index has a broader spectral peak near 3–7 yr. This problem is known to occur in AOGCMs with ECHAM4 as the atmospheric component. Guilyardi et al. (2003) discussed this problem by comparing the El Niño characteristics in AOGCMs with the same AGCM (ECHAM4-T30 or T42) but different ocean GCMs (ORCA, OPA or OPYC3) and proposed that a stronger than observed Walker circulation (or stronger trade winds) might be an important factor to cause such a high-frequency ENSO (Fedorov and Philander, 2000). Guilyardi et al. (2004) presented a new modular approach to investigate the respective role of the atmosphere and ocean in El Niño simulations of AOGCMs and found a dominant role of the atmospheric resolution in controlling the El Niño frequency; that is, the higher the model resolution, the lower the El Niño frequency. Latif et al. (2001) found too regular occurrences of the ENSO in many AOGCMs. They pointed out that its cause is still unclear and other factors can play a role, such as the noise level of the atmospheric component (Blanke et al., 1997; Eckert and Latif, 1997) or the phase-locking of the ENSO to the annual cycle (Chang et al., 1994).

Figure 2 also indicates that the model has more energy at time-scales shorter than 3 yr and less energy at the time-scale of 4–7 yr. This is statistically significant at the 94% confidence level (ln 2/11 sections) following the formula of Gillett et al. (2000). The reason for this is not known and needs further analysis.

3.2. ENSO structure in the equatorial pacific

3.2.1. SST climatology and variability. Figure 3 shows the annual mean SST and the variability of SST anomalies at the equatorial Pacific (between 2°S and 2°N) for ECHO-G CTL and the GISST2.2 observations. The model is capable of simulating the SST climatology. The warm pool in the western Pacific, the cold tongue in the east Pacific and the zonal SST gradient (with a magnitude of about 0.4°C per 10° longitude) in the central part of the basin are realistically simulated. This is consistent with previous results that generally flux-adjusted models have better skill in simulating the SST climate and gradients, although the flux adjustment does not guarantee a better simulation (Latif et al., 2001; AchutaRao and Sperber, 2002; Davey et al., 2002). The warm SST bias of about 1.5°C that appears near the eastern boundary in Fig. 3a is a common error in many AOGCMs typically linked to problems in simulating stratus clouds and coastal upwelling (Mechoso et al., 1995; Latif et al., 2001; AchutaRao and Sperber, 2002; Davey et al., 2002).

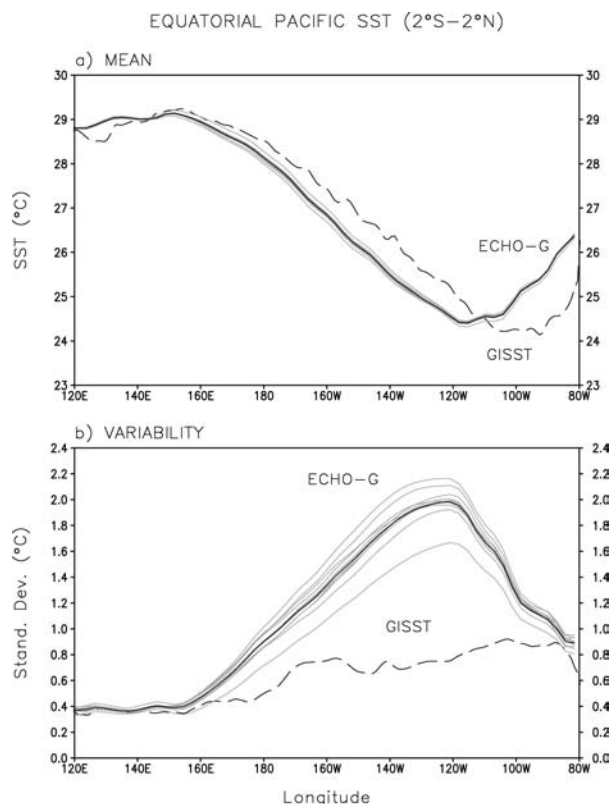


Fig. 3. Climatological mean SST (a) and standard deviation of SST anomalies from monthly mean climatology (b) in the equatorial Pacific (2°S–2°N) for ECHO-G CTL and GISST2.2 (1903–1994). Light solid lines represent the results from 10 92-yr subsections of ECHO-G CTL.

The STDs of the observed and simulated SSTs shown in Fig. 3b are calculated after removing the seasonal cycle. The observed profile shows a small variability of 0.4°C in the western Pacific and starts to increase at 160°E to a maximum value of 0.9°C at 105°W. ECHO-G also has smaller values in the western part and larger values in the eastern part, but overestimates the variability in the central and eastern Pacific with a maximum 2.0°C near 125°W. AchutaRao and Sperber (2002) reported that most (13 from 17) AOGCMs underestimate the SST variability in the eastern Pacific except for four models (ECHAM4/OPYC3, HadCM3, DOE-PCM and CERFACS), of which ECHAM4/OPYC3 is the only model with flux adjustment. Considering that ECHO-G exhibits features very close to those of ECHAM4/OPYC3 in the simulation of SST variability (i.e. both models use only annual mean flux adjustment for heat and moisture and no flux adjustment for momentum), there might be a potential influence of the flux-adjustment method on the strength of simulated SST variability.

3.2.2. Seasonal cycle of SST, zonal wind stress, and ITCZ. The seasonal cycle of the equatorial Pacific SST involves complex dynamic and physical interactions between atmosphere, ocean and land, and therefore provides a criterion for the overall

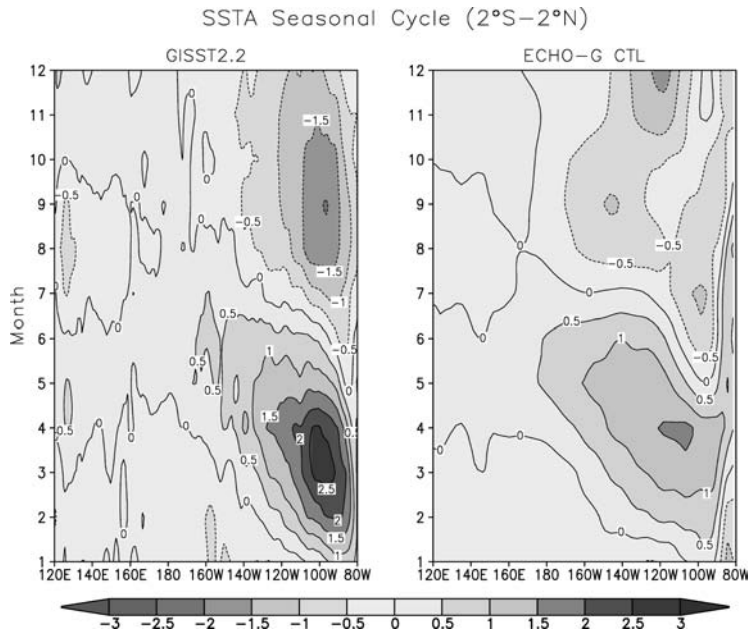


Fig. 4. Annual cycle of equatorial (2°S – 2°N) Pacific SST anomalies ($^{\circ}\text{C}$) for ECHO-G CTL (right) and GISST2.2 (1903–1994, left).

skill of coupled models in the tropics (Latif et al., 2001). Figure 4 shows the annual cycle of SST about the annual mean depicted in Fig. 3a at the equatorial Pacific for ECHO-G CTL and the GISST2.2 observations. The observed annual cycle is represented by three characteristics. The first is an annual harmonic variation with large amplitude in the eastern Pacific with a range of about 4.5°C , a maximum in March ($> +2.5^{\circ}\text{C}$) and a minimum ($\sim -2^{\circ}\text{C}$) in September. The second is a semi-annual harmonic with smaller amplitude in the western Pacific with two positive phases in April–May and October–November and two negative phases in June–September and December–February. The third is a westward propagation of SST in the central and eastern Pacific. ECHO-G captures these three observed features reasonably well, except that the range of the seasonal cycle is smaller ($\sim 3^{\circ}\text{C}$) in the eastern Pacific and that the minimum SST appears later in November–December and positioned about 20° westward compared with observations. According to previous work, many AOGCMs simulate too weak annual cycles in the eastern Pacific (Mechoso et al., 1995; Latif et al., 2001). A high resolution of the ocean component is a necessary (but not sufficient) condition for a good simulation of the SST annual cycle, and flux-adjusted models are generally able to simulate the amplitude and phase of the seasonal cycle better, although there are exceptions (AchutaRao and Sperber, 2002). Because ECHO-G is categorized into AOGCMs with a high-resolution ocean model (higher than one degree) and flux adjustment (annual mean only), the good performance of ECHO-G in the simulation of SST seasonal cycle corroborates these previous findings.

Figure 5 shows the annual mean climatology and the seasonal cycle of zonal wind stress in the equatorial Pacific for ECHO-

G CTL and the SOC observations. The SOC climatology is an average for 1980–1993 (Josey et al., 1999) whereas ECHO-G climatology is for the 1000 yr along with 14-yr averages for 71 subsections. The overall pattern of zonal wind stress including the location of maximum values near 150°W are well reproduced by ECHO-G but the simulated amplitude is larger (0.075 N m^{-2}) than the observational value (0.05 N m^{-2}). Davey et al. (2002) showed that AOGCMs without flux adjustment tend to have too weak easterly wind in the central equatorial Pacific and that flux-adjusted AOGCMs have quite similar gradients of zonal wind stress although the maximum strength ranges from 0.04 to 0.08 N m^{-2} . When compared with the 23 AOGCMs used in Davey et al. (2002), ECHO-G simulates the strongest easterlies in the equatorial Pacific along with ECHAM4/OPYC3 (0.08 N m^{-2}). This suggests that the atmospheric component plays a crucial role in setting up the zonal wind stress in the equatorial Pacific in coupled models. In addition, as discussed above, the strong zonal wind stress (strong Walker circulation) might be related to the frequent and regular ENSO in ECHO-G.

The lower panel of Fig. 5 shows the observed and simulated seasonal variation of the zonal wind stress. The observations exhibit a clear westward propagation of zonal wind stress; a positive zonal wind deviation (weaker easterlies) in the eastern Pacific in February–March moves to the western Pacific by October–November and a negative deviation (stronger easterlies) in 180 – 150°W in January moves to the western boundary by August–September. ECHO-G is not capable of simulating the annual cycle or propagation of zonal wind stress. A semi-annual cycle dominates in the western Pacific with stronger amplitudes (maximum larger than 20 N m^{-2}) than observed ($\sim 10 \text{ N m}^{-2}$). The problem of the erroneous semi-annual component in the

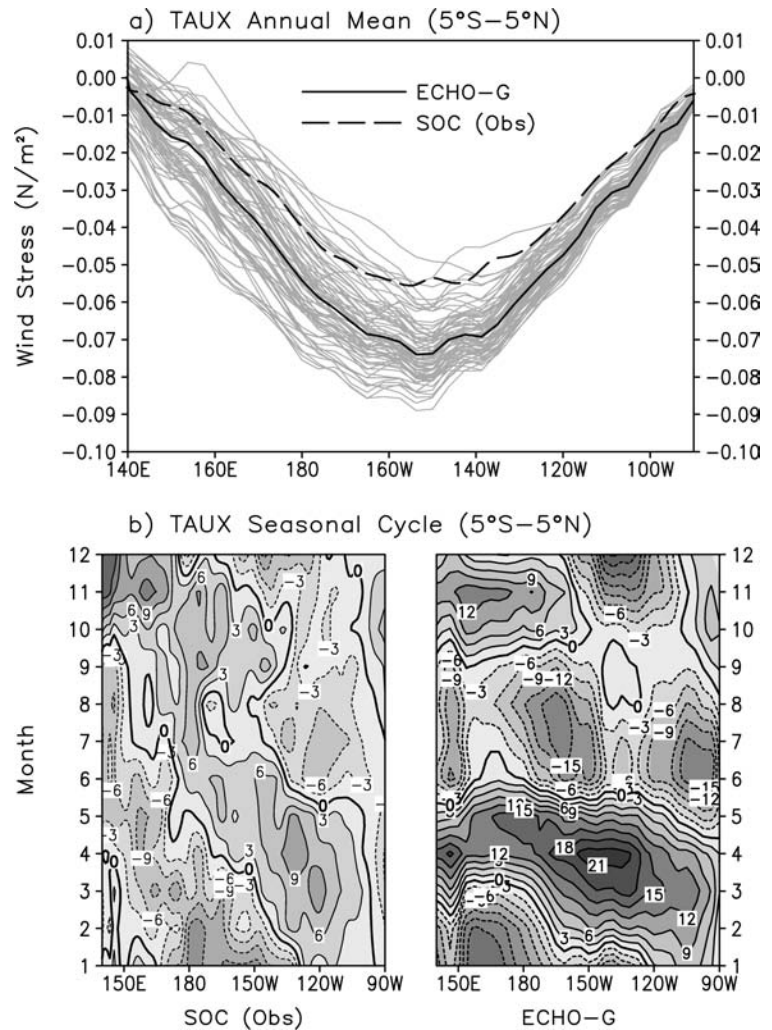


Fig. 5. Longitudinal annual mean (a) and annual cycle distribution (b) of zonal wind stress (N m^{-2}) in the equatorial (5°S – 5°N) Pacific for the SOC observation (1980–1993, left) and ECHO-G CTL (right). Light solid lines in (a) represent the results from 71 14-yr subsections of ECHO-G CTL.

zonal wind annual cycle is found in several AOGCMs (Davey et al., 2002).

Mechoso et al. (1995) have shown that many AOGCMs simulate too narrow, strong and westward extended cold tongues and too warm SSTs south of the equator in the eastern Pacific region, and that this is in some models accompanied by a double ITCZ or a migrating ITCZ across the equator in the eastern Pacific. When SST patterns in the tropical Pacific simulated in ECHO-G are compared with GISST2.2 observations for each season (Fig. 6), it is found that ECHO-G can simulate seasonal SST patterns very realistically including the zonal and meridional extent of the warm pool and the cold tongue. There is a good consistency between model and observation: almost no cold tongue in MAM, strong south-east cold tongue in SON extending westward to the date line, and the largest warm pool in SON. However, the cold tongue and associated warm tongue south of the equator are narrower meridionally in ECHO-G than in the GISST2.2 data. In order to see the behaviour of the ITCZ in ECHO-G CTL, the observed and simulated seasonal cycles

of PCP over the eastern Pacific (averaged between 150°W and 100°W) against latitude are compared in Fig. 7 (also see figs. 9 and 10 in Paper I). The observations reveal a single ITCZ located persistently between 5°N and 15°N with maximum values ($\sim 10 \text{ mm d}^{-1}$) near 10°N in June–August (Fig. 7b). ECHO-G catches the observed single ITCZ reasonably well (Fig. 7a). It shows no migration across the equator, although a weak double ITCZ can be found in February–March. However, the simulated amplitude of the ITCZ is weaker with maximum values of $\sim 6 \text{ mm d}^{-1}$, and the maximum PCP rate appears in October–November, later than in the observations. This relatively good simulation of the ITCZ and South Pacific Convergence Zone (SPCZ) in ECHO-G can be attributed to the ECHAM4 physics, i.e. the convection scheme based on the convective instability and buoyancy closure as discussed in Roeckner et al. (1996); see also Frey et al. (1997).

3.2.3. ENSO phase-locking to the annual cycle. The interannual STD of SST anomalies in the NINO3 region for each calendar month is shown in Fig. 8. It demonstrates the phase-locking

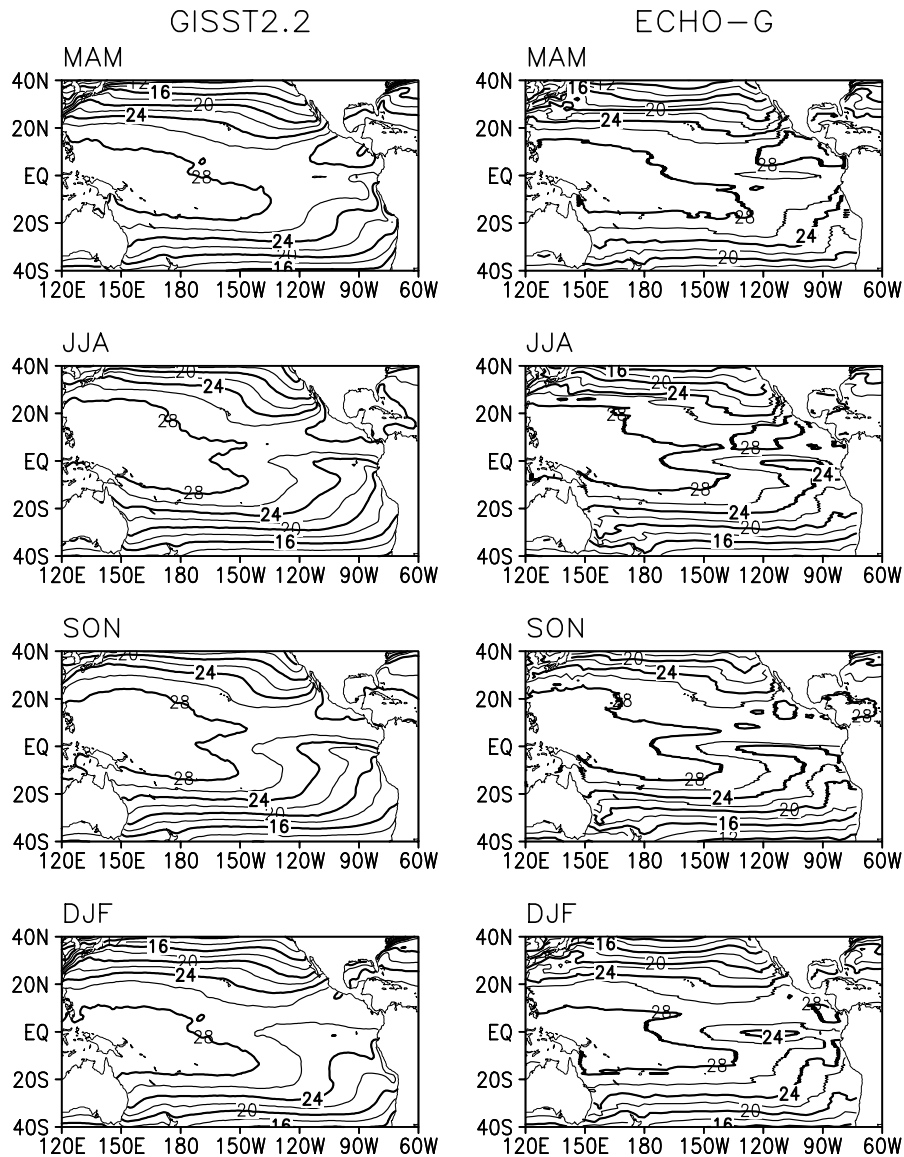


Fig. 6. The climatology of seasonal mean SST ($^{\circ}\text{C}$) in the tropical Pacific for ECHO-G CTL (right) and GISST2.2 (1903–1994, left).

of the ENSO to the annual cycle. The observed STD exhibits a maximum in December ($\sim 0.9^{\circ}\text{C}$) and a minimum in April ($\sim 0.5^{\circ}\text{C}$), which means that peak ENSO events occur in the NH winter. ECHO-G captures the pronounced winter maximum and spring minimum, but the maximum is reached too early in July with overestimated amplitude and is maintained until the next January. AchutaRao and Sperber (2002) have shown that most AOGCMs taking part in CMIP1 have weak variability and no seasonal peak at all, and that only three models (ECHAM4/OPYC3, HadCM2 and HadCM3) simulate reasonably well the phase and amplitude of the interannual variability of ENSO. Because there is no systematic relation between the simulation of a realistic SST annual cycle and the simulation of ENSO phase-locking to the annual cycle (Latif et al., 2001), ECHO-G is evaluated to

have good skill in simulating both the SST annual cycle (Fig. 4) and the ENSO seasonal cycle phase-locking (Fig. 8) compared to other models.

3.2.4. Ocean subsurface behaviour. In order to investigate the ocean subsurface behaviour in ECHO-G CTL, correlations between the NINO3 index and thermocline depth are computed over the equatorial and off-equatorial bands with a varying time lag up to ± 24 months and are compared with the observed pattern in Fig. 9. The depth of the 20°C isotherm (Z20) is used as a thermocline depth proxy. The observed Z20 is calculated from the SIO upper ocean temperature data set (Table 1) through linear interpolation in the vertical (Rodgers et al., 2004). The observed correlation between the NINO3 index and Z20 shows a larger positive coefficient in the equatorial eastern Pacific at zero lag,

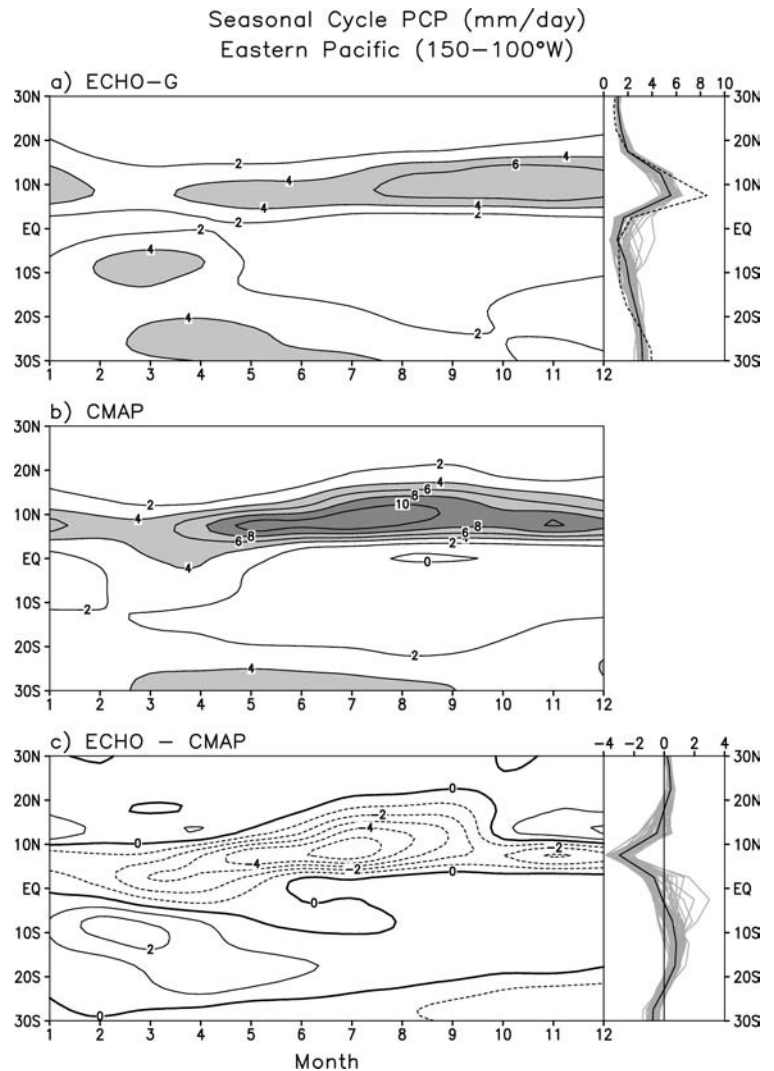


Fig. 7. Annual cycle of PCP (mm d^{-1}) in the tropical eastern Pacific ($150\text{--}100^\circ\text{W}$) for ECHO-G CTL (a), CMAP (1979–1998) (b), and their difference (c). Zonal means of the model (solid line) and the observation (dashed line) are plotted together in the right upper panel. The zonal mean of model biases is shown in the right lower panel. Light solid lines in zonal mean plots represent the results from 50 20-yr subsections of ECHO-G CTL.

implying that the SST anomalies are closely linked to variations of the local thermocline depth in the region (Fig. 9a). The equatorial Z20 anomalies propagate eastward with a period of about 4 yr. The observed off-equatorial Z20 exhibits a westward propagation with the same sign as equatorial patterns at zero lag (Fig. 9c). This correlation structure is consistent with the eastward (westward) propagation of the equatorial Kelvin (off-equatorial Rossby) wave, its reflection into the Rossby (Kelvin) wave in the eastern (western) Pacific, and its subsequent westward (eastward) propagation, giving the basis for the well-known delayed oscillator theory (e.g. Suarez and Schopf, 1988).

ECHO-G CTL reproduces well the observed high correlation at zero lag in the equatorial eastern Pacific and its eastward propagation from the West Pacific (Fig. 9b). The westward propagation of the off-equatorial Z20 anomalies is also simulated well (Fig. 9d), supporting that the equatorial wave dynamics as the basic ENSO mechanism is captured in the coupled model (e.g. Neelin et al., 1998). However, the simulated oscillation period

of 2 yr is too short, consistent with the overestimated power in the NINO3 index (Fig. 2). Therefore, also too strong correlations appear around 1-yr lag over a large area of the basin (Figs. 9b and d). These two shortcomings are common problems found in many coupled models (Latif et al., 2001) and an important role of the atmospheric resolution has been suggested on controlling the ENSO frequency (see discussion above).

3.3. *El Niño* response

In this section, simulated and observed atmospheric responses to the ENSO are compared with the help of correlation and regression patterns for T2m, PCP and MSLP with the NINO3 index for the December–February (DJF) season when the observed *El Niño* reaches its maximum amplitude (Fig. 8). Figure 10 shows the spatial distribution of correlation coefficients, while the corresponding regression maps are given in Fig. 11. HadCRUT2 is used as T2m observations for the period of 1903–1994 (Table 1),

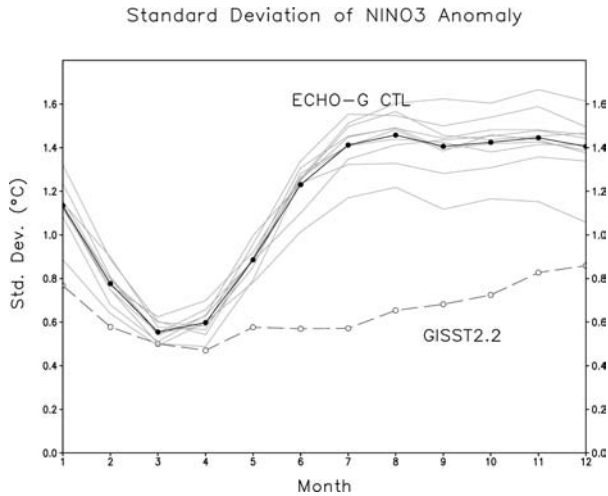


Fig. 8. Monthly standard deviation of the NINO3 SST (°C) for ECHO-G CTL and GISST2.2 (1903–1994). Light solid lines represent standard deviations from 10 92-yr sections of ECHO-G CTL and the dark solid line is a mean of the 10 standard deviations.

and grid points where the number of observations is less than 20 in DJF are treated as missing points. The observational correlations of T2m with the El Niño index are significantly positive over the tropical central and eastern Pacific, northern North America, the west coast of North and South America, the Indian Ocean and southern Africa, while significant negative values appear in the central North Pacific and southern North America. For the 999 DJF means of ECHO-G, the threshold for significant correlation coefficients is 0.06 (0.08) at the 10% (5%) significance level (two-tailed *t*-test). The ECHO-G correlation pattern (Fig. 10a) captures the observed features of the ENSO-related T2m pattern

well, except that the region with positive values in the central equatorial Pacific extends more to the west and the correlation is higher over northern North America, northern South America and the Indian Ocean. Also, ECHO-G does not simulate realistically the observed symmetry of the T2m response to the ENSO about the equatorial Pacific (Trenberth and Caron, 2000). The regression map of T2m with the NINO3 index (Figs. 11a and b) shows that, during El Niño events, the region with anomalously warm T2m in the tropical Pacific in ECHO-G is more confined to the equator and extends more eastward towards Brazil. The region with positive regressions over northern North America is shifted north-westward compared to the observations with a maximum near Alaska. Overall, however, scales and patterns are well reproduced.

The observed correlation pattern of the DJF PCP with the NINO3 index (Fig. 10d) is more localized or noisier than the T2m and MSLP patterns. Because only 15 DJF (1979/1980–1993/1994) CMAP data are used to calculate the correlation coefficients, a statistically significant correlation is obtained only above 0.51 (0.64) at the 10% (5%) significance level. During El Niño events, PCP above average occurs in the tropical central and eastern Pacific, south-eastern Pacific, south-eastern North America, and at the west coast of North America, while it is statistically significant below average in the equatorial western Pacific, the tropical Pacific north and south of the equatorial larger PCP area, north-eastern Brazil and south-eastern Africa. Even if very short periods of observations are taken, the overall features are very similar to those shown previously by Ropelewski and Halpert (1987) and Trenberth and Caron (2000). ENSO-related PCP anomalies in ECHO-G CTL (Fig. 10c) exhibit a very realistic correlation pattern compared with observations, especially the merging of ITCZ and SPCZ into a huge convective system

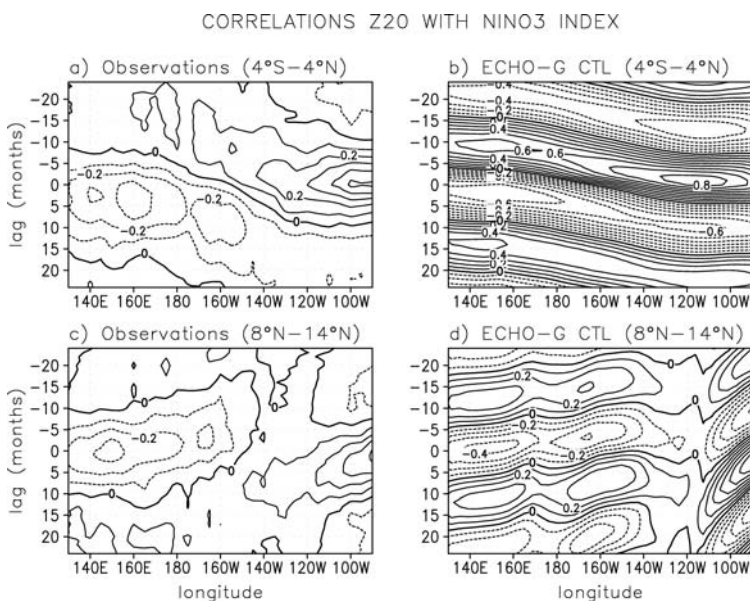


Fig. 9. Lag correlations between the NINO3 index and Z20 anomalies for observation (left) and ECHO-G CTL (right) averaged over equatorial and off-equatorial latitude bands as indicated. Positive (negative) lags mean that Z20 (NINO3 index) leads. Contour intervals are 0.1 in all panels.

DJF NINO3 SST Correlation

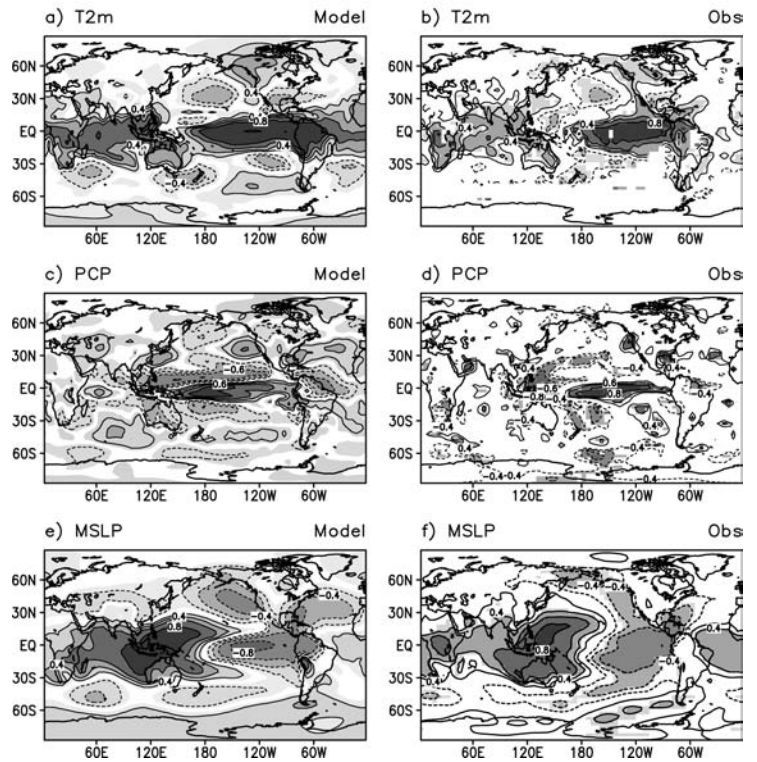


Fig. 10. Correlation coefficients of DJF mean T2m (top), PCP (middle) and MSLP (bottom) with the DJF mean NINO3 index for ECHO-G (left) and observations (right). Contour intervals are 0.2 and zero lines are omitted. Contour lines of -0.2 and $+0.2$ are additionally left out in (d). Shadings indicate areas where the correlation coefficients are statistically significant at 95% level (two-tailed t -test).

DJF NINO3 SST Regression

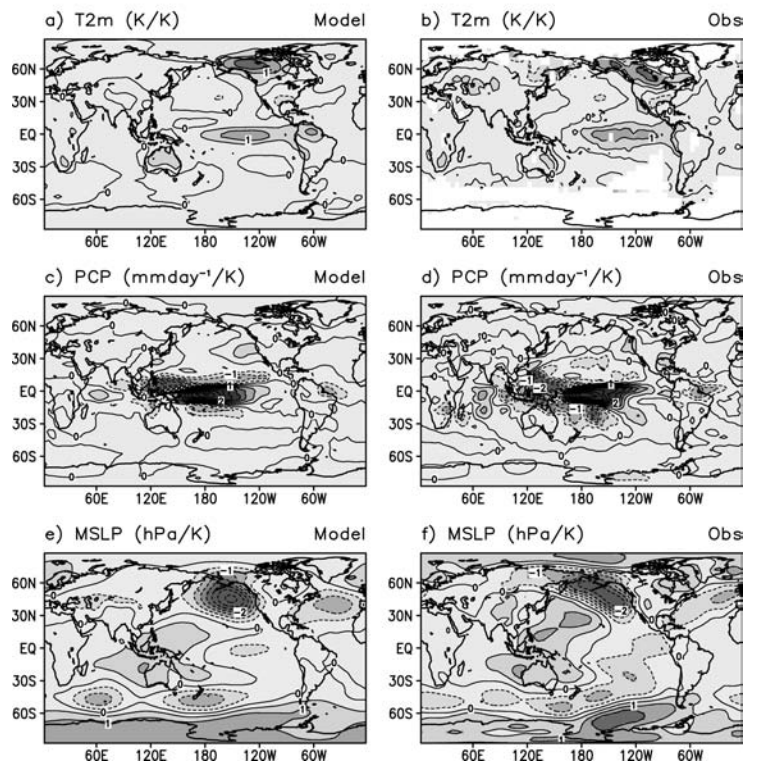


Fig. 11. Same as Fig. 10 but for regression coefficients. Contour intervals are 0.5.

centred at the equator in the mature phase of the ENSO (Roeckner et al., 1996; Trenberth and Caron, 2000) is well reproduced. However, positive correlations in the equatorial central Pacific extend more westward and south-eastward off the west coast of South America, and the negative correlations in the tropical Pacific of both hemispheres are more trapped near the equator than observed (compare also the regression maps in Figs. 11c and d). This is closely linked with the problem of T2m response (Figs. 10a and b). PCP regressions in Figs. 11c and d show that the amplitudes of PCP changes related to the ENSO are reasonable in ECHO-G CTL.

In the observed correlation of the MSLP with the NINO3 index (Fig. 10f), the apparent response of atmospheric mass to the ENSO is characterized by an oscillation between two centres of action: the Indonesian centre and the tropical Pacific centre. The statistically significant correlation is 0.33 (0.42) at the 10% (5%) significance level for the 36 DJFs of the MSLP fields of NCEP/NCAR reanalysis from 1958/1959 to 1993/1994. The Indonesian centre of action extends into Africa and the tropical Atlantic, while the tropical Pacific centre of action extends northward into the North Pacific (Fig. 10f). The regression map for the observed MSLP shows larger variation of the ENSO-related MSLP over the North Pacific and South Pacific at high latitudes than in the tropics (Fig. 11f). The MSLP response to the ENSO in ECHO-G CTL resembles the observational field nicely (Fig. 10e). Correlation fields in the model display a good location of the two centres of action although shifted westward about 10° – 20° . The correlations in the model are stronger than observed in the central equatorial Pacific (and more confined to the equator, similarly to the patterns of T2m and PCP), over Indonesia, the Indian Ocean and the west coast of North America, whereas they are weaker over central Africa and the tropical Atlantic. Regression maps of the MSLP in Fig. 11e show that the magnitude of the MSLP response to the ENSO in the model is reasonable, including the deepening of the Aleutian Low and its south-eastward displacement (van Loon and Madden, 1981; Roeckner et al., 1996). However, the negative anomaly in the North Pacific is stronger and broader, and the positive anomaly in the western tropical Pacific does not extend sufficiently north-eastward in ECHO-G.

A common problem with coupled models is that the Southern Oscillation and warming in the eastern tropical Pacific seem to occur in an uncoordinated fashion (e.g. AchutaRao and Sperber, 2002). In this respect, a simple analysis of ECHO-G CTL shows that the DJF SOI is highly correlated with the NINO3 index (the correlation coefficient is -0.69 for 999 DJFs) although the simulated linkage is somewhat weaker than observed (the correlation coefficient is -0.78 for 1903/1904–1993/1994). Owing to the high correlation between the two indices, the simulated ENSO-related patterns (correlation and regression maps of T2m, PCP and MSLP) based on the SOI index are very similar to those from the NINO3 index (not shown). It is also found that DJF composites of the three atmospheric variables for the warm

event, defined as in the NINO3 index ≥ 0.6 and SOI ≤ -0.6 as in AchutaRao and Sperber (2002), resemble the regression map with the NINO3 index (Fig. 11) for ECHO-G CTL (not shown).

In summary, the atmospheric response to the ENSO in ECHO-G CTL indicates that ECHO-G can be classified into the category Group I defined by AchutaRao and Sperber (2002), containing the models which are most consistent with observations. The AOGCMs in Group I (ECHAM4/OPYC3, HadCM2, CERFACS, DOE-PCM and HadCM3) have a well-defined Walker circulation, enhanced warming extending from the tropical central Pacific to the west coast of South America, and associated rainfall in the tropical Pacific (AchutaRao and Sperber, 2002). While ECHAM4/OPYC3 and CERFACS simulate a warming displaced further to the north-east over Hudson Bay and Greenland and the other three AOGCMs in Group I have a cooling over North America (AchutaRao and Sperber, 2002), ECHO-G simulates the warming over North America quite well (Fig. 11a). Therefore, ECHO-G can be considered to have good skill in simulating the atmospheric response to the ENSO compared with other AOGCMs.

4. North Atlantic Oscillation

4.1. Wintertime MSLP variability in the NH

The NAO is one of the major internal climate variability signals in the NH extratropics with monthly to decadal time-scales, and exerts a strong influence on the climate of the Euro-Atlantic and Pacific regions (Thompson and Wallace, 2001). Various methods have been proposed to define an NAO index, e.g. the pressure difference between stations on the Azores and Iceland (Rogers, 1984; Hurrell, 1995; Jones et al., 1997), the leading PC time series of the NH MSLP field (Rogers, 1990; Thompson and Wallace, 2000, 2001), or the first PC of time series of intensity and latitudinal position of the Azores High (AH) and the Icelandic Low (IL; Glowienka-Hense, 1990; Paeth et al., 1999). In this section, we compare the simulated NAO with the observed NAO using the station-based NAO index (Gibraltar minus Iceland DJFM mean MSLP) of Jones et al. (1997). In addition, we compare the station-based simulated NAO index with the PC-based one. The spatial structure is examined by comparing local patterns of observed and simulated interannual variability of MSLP.

Figure 12 shows maps of the interannual variability or STD of the DJFM MSLP in the NH extratropics (20° – 90° N) for ECHO-G CTL and NCEP/NCAR reanalyses. In contrast to fig. 14 of Paper I (global map of STD of annual mean MSLP) the linear trend is not removed in order to retain the decadal variability. The observed pattern in Fig. 12b exhibits two centres of action with large variability (>5 hPa) situated over the northern North Atlantic and the North Pacific. The North Atlantic centre broadly extends to the Arctic Ocean. The simulated MSLP variability reproduces well the observed location and strength of the two

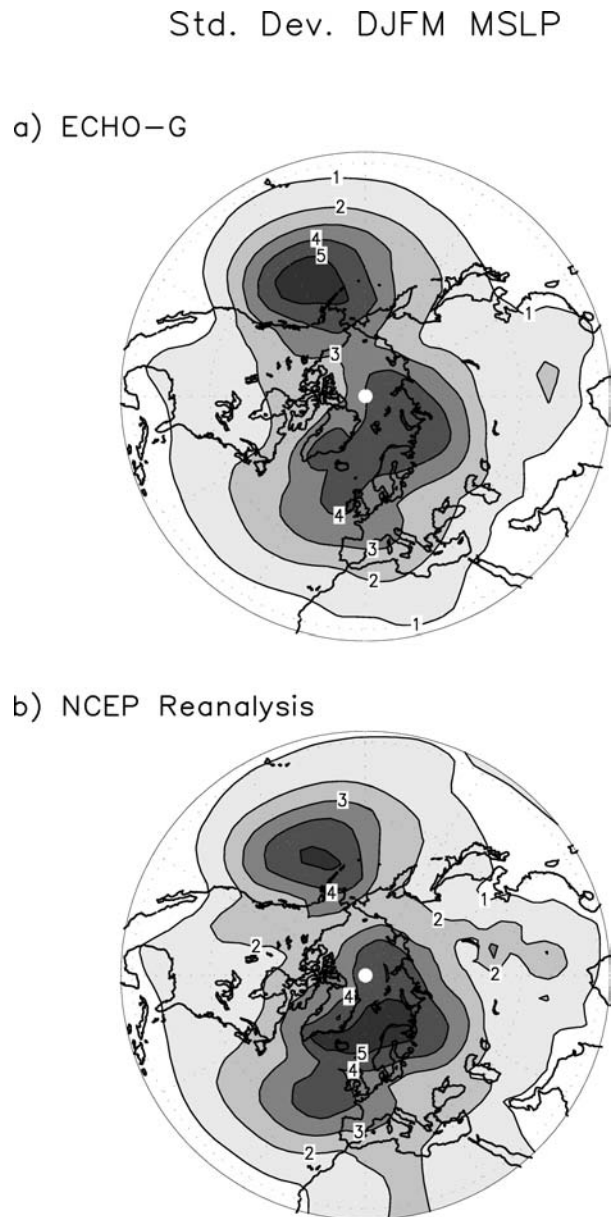


Fig. 12. Spatial distribution of interannual standard deviation of DJFM MSLP (hPa) from ECHO-G CTL (a) and NCEP/NCAR reanalysis (1958/1959–2000/2001) (b).

centres, but the simulated variability in the Atlantic sector is somewhat (~ 1 hPa) weaker than observed (Fig. 12a). As in figs. 12a and b of Paper I, the wintertime mean MSLP pattern is reasonably well simulated in ECHO-G CTL including the position of IL although the simulated AH is stronger and shifted towards the east.

The eigenvector pattern and time series of the leading PC of the DJFM MSLP in the NH extratropics for the NCEP/NCAR reanalyses (1958/1959–2000/2001, 43 DJFMs) are shown in Fig. 13. The time series of the station-based NAO index (Jones

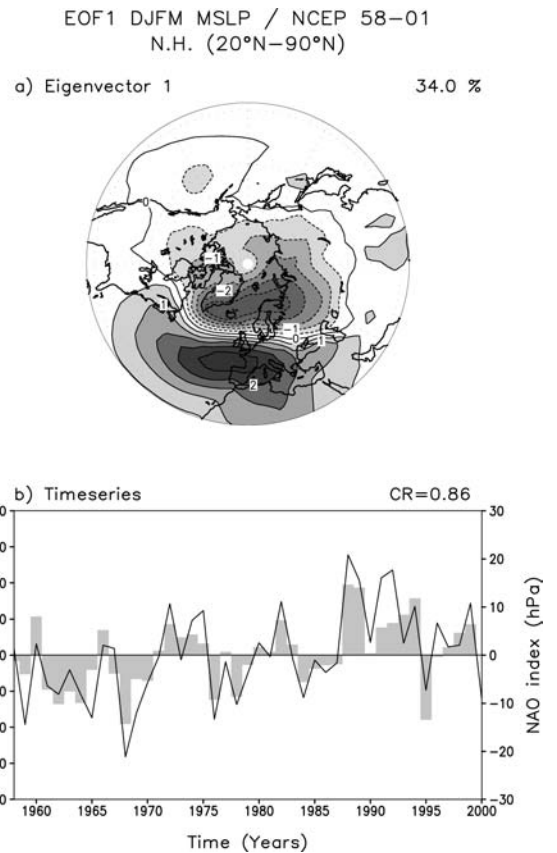


Fig. 13. The leading PC of DJFM MSLP from NCEP/NCAR reanalysis (1958/1959–2000/2001): eigenvector (a) and PC time series (solid line) (b). Bars in (b) represent the NAO index anomaly (hPa) which is defined as the Gibraltar minus Iceland DJFM mean MSLP difference (Jones et al., 1997). The eigenvector in (a) has a unit of hPa by multiplying PC standard deviation to normalized eigenvector.

et al., 1997) is drawn together with the PC time series for better comparison. The very high correlation (0.86) between the PC time series and the NAO index indicates that the leading PC mode of the MSLP corresponds to the NAO mode. It explains 34.0% of the DJFM MSLP interannual variability in the NH extratropics. The observed PC spatial pattern is characterized by a dominant north–south dipole structure in the North Atlantic sector. The dipole represents the well-known strengthening (weakening) of AH and IL (or pressure gradient and zonal wind advection from the Atlantic into western Europe) in the positive (negative) NAO phase. It is notable that there is no Pacific centre of action in the observations used here (Fig. 13a), differently from the leading empirical orthogonal function (EOF) mode of Thompson and Wallace (1998) where an additional centre of action over the North Pacific is found (see fig. 1 of Thompson and Wallace, 1998). However, Thompson and Wallace (1998) could obtain the Pacific centre of action for the last 30 yr (1968–1997) only after removing the linear trend for each grid point, because the MSLP decreasing trend over the North Pacific for this period is strong

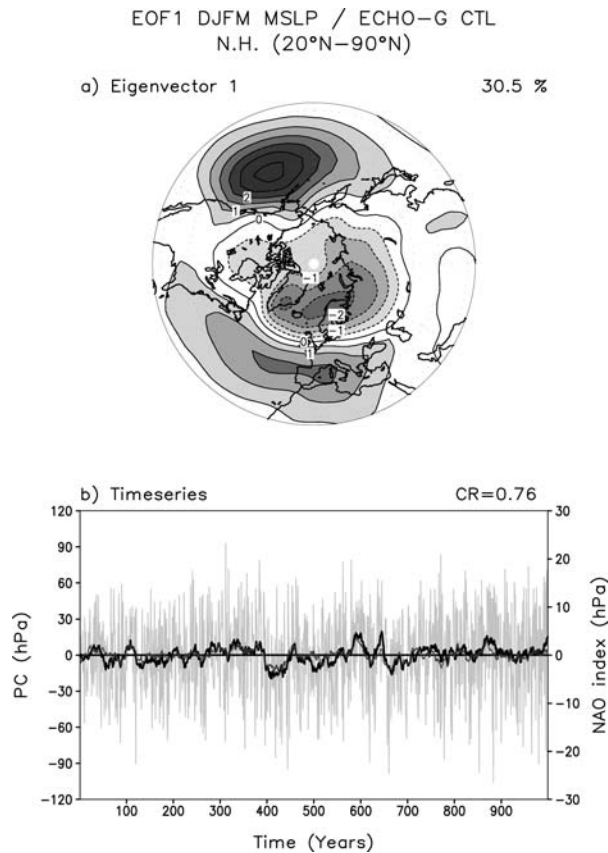


Fig. 14. Same as Fig. 13 but for DJFM MSLP from ECHO-G CTL (999 DJFMs). In (b) the light line is the PC, the thick dark line is an 11-yr moving average of the PC, and the thin dark line is an 11-yr moving average of the NAO index anomaly (hPa).

enough to cancel the centre of action over the North Pacific in their EOF of wintertime mean MSLP.

Figure 14 shows the simulated leading PC of the wintertime MSLP. The percentage of explained variance is 30.5%, close to the observed 34.0%. This mode represents NAO variability in ECHO-G CTL because the PC time series is positively correlated (0.76) with the station-based NAO index. The spatial pattern of the corresponding eigenvector shows a dipole structure in the Atlantic sector similar to that observed, but its amplitude is about half of the observed value only. The main weakness of the simulated PC pattern is that too strong variability appears in the North Pacific, which is not found in the observational PC pattern (Fig. 13a). Also, too strong negative correlations (-0.29 , significant at 99% confidence level) between the DJFM NINO3 and NAO indices is found in the model simulations, while there is almost no correlation observed, e.g. -0.05 for 92 DJFM observations (1903–1994). Stephenson and Pavan (2003) also addressed a very low observational correlation ($+0.02$) between the DJF NINO3 and NAO indices (1900–1991). The EOF result for the 3- or 5-yr low pass filtered MSLP

of ECHO-G CTL shows that the centre of action in the North Pacific is weakened but still has an amplitude comparable to that in the North Atlantic. This means that the dominant North Pacific variability in ECHO-G CTL might not be excited by the strong and regular ENSO variability (see Section 3). Rather this mode belongs to the common error seen in other AOGCMs such as ECHAM3/LSG (Timmermann et al., 1998), HadCM2 (Osborn et al., 1999), HadCM3 (Collins et al., 2001), CCSM2 (Holland, 2003), ECHAM4/OPYC3, NCAR CSM, and CCSR (Stephenson and Pavan, 2003). Stephenson and Pavan (2003) speculated that an overly strong teleconnection between the tropics and the extratropics might cause the problem.

The 11-yr running mean time series of the leading PC of the model MSLP reveals long-term variations with decadal to centennial time-scales (Fig. 14b), trends of which will be compared with the observed change of the NAO index (Fig. 13b) below in the context of the detection of human impacts.

4.2. Power spectrum and trend analysis of the NAO index

Figure 15 shows the time series of station-based NAO index anomalies for 999 DJFM ECHO-G CTL and 177 DJFM observations (1825/1826–2001/2002). The DJFM MSLP difference (Gibraltar minus Iceland; Jones et al., 1997) is defined as the NAO index for both data sets. There is almost no long-term trend in the model NAO (-0.022 hPa per century) whereas the observations have a weak increasing trend of 0.11 hPa per century. The observed magnitude of the NAO trend seems to be within the model internal variability. When the amplitude of the NAO variability is estimated from standard deviations in the detrended time series, the model NAO amplitude (~ 5.5 hPa) is somehow smaller than that observed (~ 6.4 hPa). Distinct decadal variability can be seen in both data sets.

Power spectra of the simulated and observed linearly detrended NAO index are shown in Fig. 16. The model period of 999 DJFMs is divided into five 177-yr subsections and the power spectra obtained from the five subsections are averaged to define the mean spectrum of the model data. The observed spectrum indicates near-white behaviour with no significant spectral peaks, meaning that there is no periodic signal in the observed NAO. Osborn et al. (1999) have pointed out that the observed spectral shape for NAO varies highly between definitions. The NAO index of Jones et al. (1997), used in this study, exhibits a spectrum close to white noise while the Azores minus Iceland version produces a redder spectrum (see Hurrell and van Loon, 1997; Wunsch, 1999; Stephenson et al., 2000). The NAO spectrum simulated by ECHO-G exhibits a very similar flat behaviour with no preferred time-scale, although there exist a couple of spectral differences for long-term scales (>40 yr) and near 8-yr periods between the simulated and observed NAO variability.

Using the simple detection method defined by Collins et al. (2001) and for global mean T2m in section 3.1 of Paper I, the

Fig. 15. Time series of DJFM mean NAO index anomalies (thin lines) from ECHO-G CTL and observations (1825/1826–2001/2002). Solid lines are linear trends. Their values are given in parentheses (hPa per century). Thick lines are 11-yr moving averages.

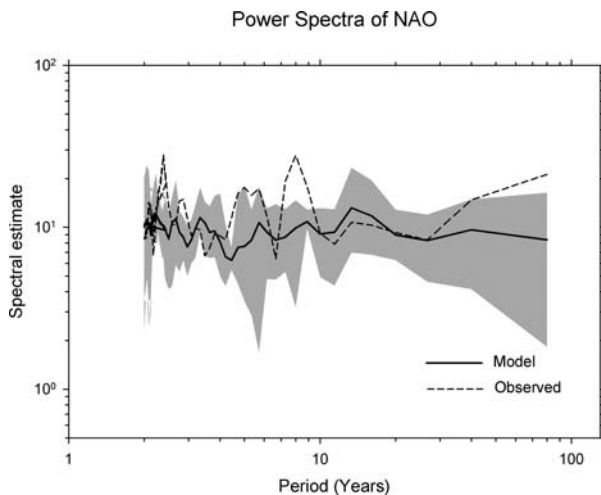
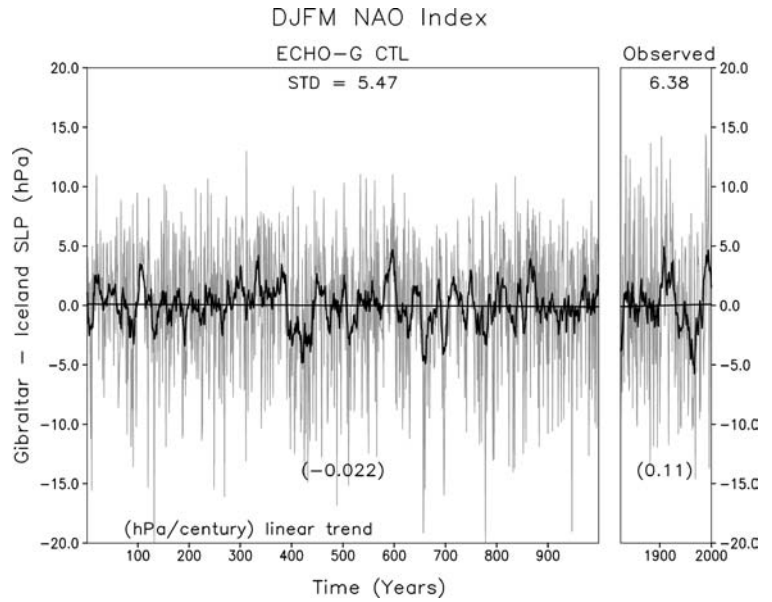


Fig. 16. Power spectra of DJFM NAO indices for observations (dashed line) and ECHO-G CTL (thick solid line). Five 177-yr sections of ECHO-G CTL are used to obtain the range (grey shading) of the model spectra.

observed and simulated NAO index trends are compared for different time-scales in Table 2. The number of simulated NAO trends larger than that observed is counted and its relative occurrence is given by dividing it by the total number of trends for each period. The observed trend in the NAO index is largest (0.25 hPa yr⁻¹) in the recent 40-yr period of 1960–1999 and the second largest trend appears as a 50-yr trend (0.18 hPa yr⁻¹) in 1950–1999. Such a large increase cannot be found in the model control run, and the 60-yr observed trend also occurs very infrequently (~0.3% chance). On the other hand, the observed trend for the recent 10–30 yr period is simulated with a chance of more than 1% by the model. This result is in accordance with previous

Table 2. Trends of the observed NAO index and corresponding trend occurrences greater than the observed trends in the ECHO-G CTL

Observation period (yr)	Trend length (yr)	Observed trend (hPa yr ⁻¹)	Model trend occurrence	
			Occurrence	Relative occurrence (%)
1990–1999	10	–0.18	623	62.9
1980–1999	20	0.12	279	28.5
1970–1999	30	0.18	66	6.8
1960–1999	40	0.25	0	0
1950–1999	50	0.18	0	0
1940–1999	60	0.11	3	0.3
1930–1999	70	0.08	10	1.1
1920–1999	80	0.02	184	20.0
1910–1999	90	0.002	483	53.1
1900–1999	100	–0.01	749	83.2
1823–1999	177	0.001	395	48.0

analyses of multicentury control runs with HadCM2 (Osborn et al., 1999) and HadCM3 (Collins et al., 2001).

Some studies provide statistical evidence that the recent NAO change might include anthropogenic effects by comparing the observed NAO trend with those from climate change simulations forced with increasing greenhouse gases (e.g. Paeth et al., 1999; Shindell et al., 1999). Other studies have suggested an important role of the tropical oceans (e.g. Hoerling et al., 2001) or of the Atlantic Ocean (e.g. Rodwell et al., 1999; Robertson et al., 2000; Paeth et al., 2003) in the decadal variations of the observed NAO. However, the question whether the observed NAO trend can be explained by natural variability or is a response to increasing concentrations of anthropogenic greenhouse gases is still largely controversial because the NAO response to

greenhouse warming is different from model to model (see, for example, Osborn et al., 1999 for the HadCM2 response, Paeth et al., 1999 for ECHAM3/LSG and ECHAM4/OPYC3, and Fyfe et al., 1999 for CGCM1), and the observed oceanic forcing contains partly an effect of greenhouse warming (Bretherton and Battisti, 2000).

4.3. NAO-related patterns of atmospheric variables

Figures 17 and 18 show the maps of correlation and regression patterns of the DJFM mean T2m, PCP and MSLP with the NAO index shown in Fig. 15 for the observations and the model CTL. HadCRUT2, CRU-PCP and NCEP/NCAR reanalysis MSLPs are

used for observational data (Table 1). In the observational data sets of HadCRUT2 and CRU-PCP, grid points where the number of DJFM mean observations is less than 20 are treated as missing points. The regression coefficients indicate the atmospheric response to one STD of the NAO index (Hurrell, 1996; Osborn et al., 1999). The observed NAO-related T2m correlation pattern in Fig. 17b is characterized by quadrupole structure over the Atlantic sector (Hurrell and van Loon, 1997; Osborn et al., 1999; Stephenson and Pavan, 2003). There are two regions with strong positive correlations (>0.3), the first centred over Scandinavia and reaching downstream into northern Russia, and the second over south-east North America, as well as two regions with negative correlations (<-0.3), one centred over the Labrador Sea

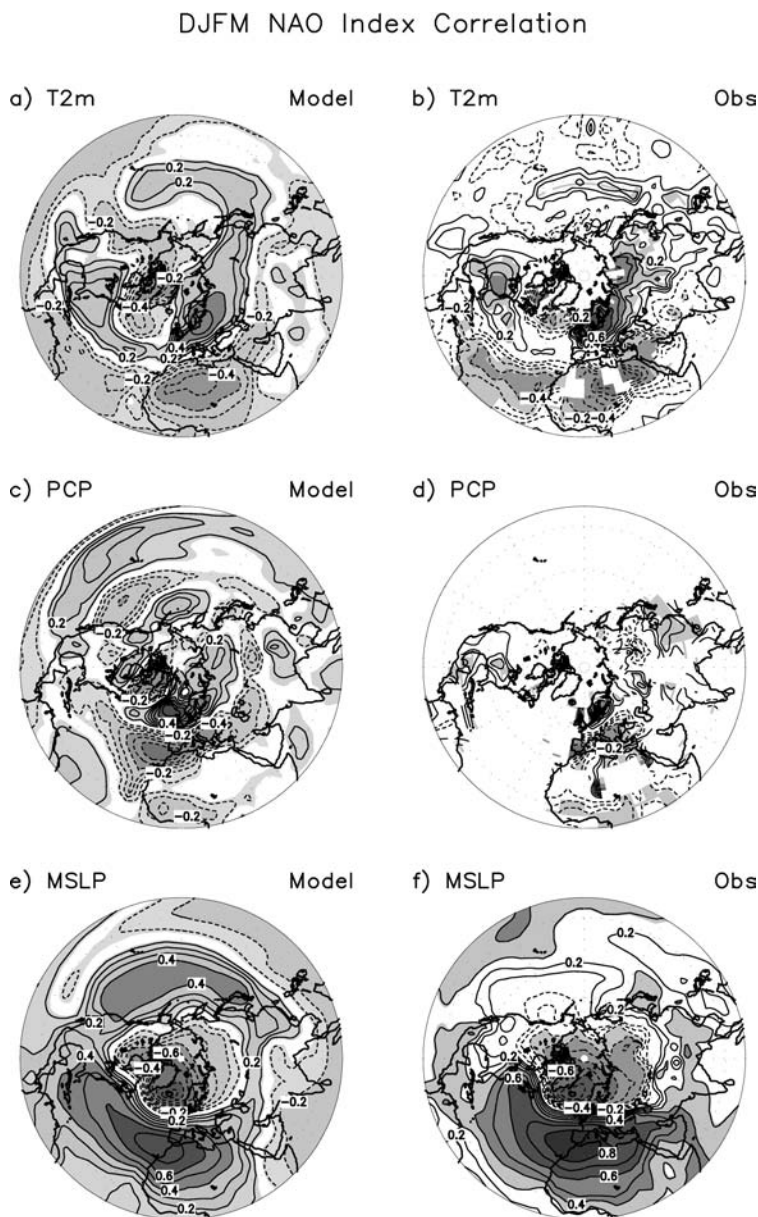


Fig. 17. Spatial distribution of correlation coefficients with the DJFM mean NAO index for the observations (right panels) and model simulations (left panels): DJFM mean T2m (top), PCP (middle) and MSLP (bottom). Contour intervals are 0.1 and zero lines are omitted. Shadings represent the areas where the correlation coefficients are statistically significant at 95% level (two-tailed *t*-test).

DJFM NAO Index Regression

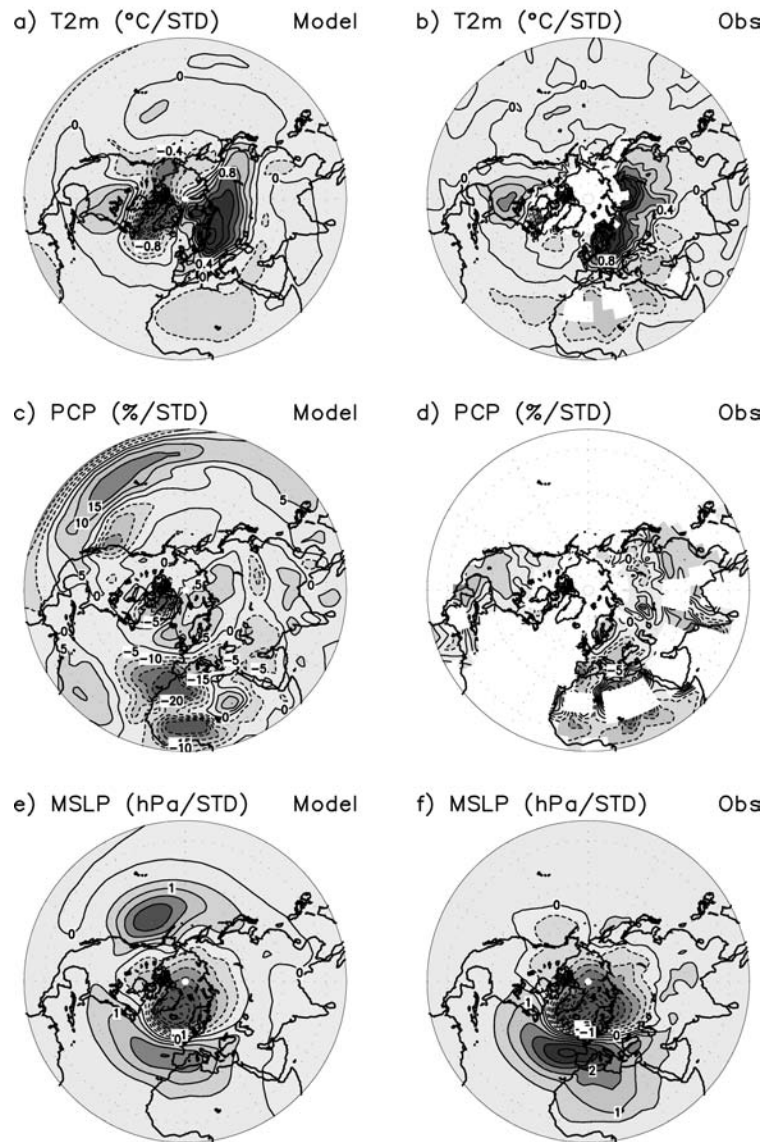


Fig. 18. Same as Fig. 17 but for the regression coefficients. Note that regression coefficients are normalized by the standard deviation (STD) of the NAO index. Contour intervals are $0.2^{\circ}\text{C STD}^{-1}$, $5\% \text{ STD}^{-1}$ and 0.5 hPa STD^{-1} for T2m, PCP and MSLP, respectively.

and the other over northern Africa (Fig. 17b). The model captures the observed quadrupole pattern realistically including the location of the above-mentioned four centres, but the simulated correlation is lower over the Eurasian sector, especially over northern Russia, and the positive correlation of south-east North America is shifted eastward relative to the observed (Fig. 17a). An observed warm response larger than $1^{\circ}\text{C STD}^{-1}$ to a positive NAO index exists over north-eastern Europe (Fig. 18b). The model regression map reproduces that observed quite well with similar amplitude, but the warming over northern Russia is smaller in the simulations (Fig. 18a). ECHO-G also shows a weakness by simulating a broad cooling response over northern Canada that extends further into Alaska than found in the

observations. Comparing the T2m correlation map of ECHO-G (Fig. 17a) with the leading eigenvectors of the T2m correlation matrix for 17 AOGCMs shown by Stephenson and Pavan (2003), the ECHO-G model shows good skill in the simulation of the T2m quadrupole pattern over the Atlantic.

The observed correlation of the PCP with the NAO index exhibits the well-known pattern of dry conditions over southern Europe and the Mediterranean and wetter-than-normal conditions over northern Europe and Scandinavia (Hurrell and van Loon, 1997) during positive NAO phases (Fig. 17d). ECHO-G reproduces the observed pattern of NAO-related PCP over Europe (Fig. 17c). However, the simulated dry area over southern Europe extends further eastward. The other observed

features involve positive correlations over southern North America and weak negative correlations over northern North America (Fig. 17d). ECHO-G cannot simulate the North American pattern correctly (Fig. 17c). The regression maps of PCP are drawn with percentage change relative to the 30-yr (1961–1990) climate for observation and the 1000-yr mean for the model data (Figs. 18c and d). The observed magnitude of PCP change associated with the NAO is well simulated by ECHO-G over Europe.

The observed correlation pattern of the MSLP with the NAO index exhibits a distinct dipole structure over the Atlantic with little correlation over the Pacific. A positive centre of correlation above 0.8 is located over Gibraltar and a negative one below -0.8 over Iceland (Fig. 17f). ECHO-G reproduces the observed dipole pattern of MSLP correlation realistically, except for the fact that the simulated correlations are weaker than observed, especially in the positive centre over Gibraltar (compare contour lines $+0.6$) and that the positive centre is positioned further westward than observed (Fig. 17e). The most evident differences between the simulated MSLP correlation map and that observed are the positive correlations larger than 0.4 south of the Aleutian Low, which extend westward over Japan, and the negative correlations stronger than 0.2 over the Indian Ocean and Indonesia, the first feature being absent while the second has a reversed sign in the observations (Figs. 17e and f). The regression maps of the MSLP support these results (Figs. 18e and f). When the NAO index is higher than normal by one STD, the observed maximum ($> +2.5$ hPa STD^{-1}) of MSLP change is located over the west Iberian Peninsula, north-west of the correlation maximum, and a minimum (< -5 hPa STD^{-1}) appears over Iceland identical to the correlation minimum (Fig. 18f). ECHO-G CTL captures the observed regression pattern but underestimates the amplitude by $1-1.5$ hPa STD^{-1} over the two centres of action and over Siberia, while it produces a too large MSLP response over the North Pacific during positive phases of the NAO. The additional North Pacific centre and therefore the more zonally symmetric pattern in the model represent a closer resemblance to the observed AO (Thompson and Wallace, 1998). This may be associated with a closer link between the NAO and the ENSO, i.e. an overestimated Atlantic–Pacific teleconnection (Stephenson and Pavan, 2003), which is an error seen in many AOGCMs as discussed in Section 4.1.

5. Discussion and conclusion

In this paper, the two dominant signals of natural climate variability (ENSO and NAO) are examined in a 1000-yr CTL with the coupled climate model ECHO-G. As a whole, it can be said that ECHO-G performs well compared to other coupled models, despite its relatively coarse resolution of the atmosphere ($\sim 3.75^\circ$), although it shares some systematic errors with other models.

It is shown that the ENSO-like variability in the model has stronger than observed amplitudes and is too frequent and regular. This is probably the reason for a too strong 2-yr peak in the

simulated global mean T2m energy spectrum and the underestimated energy at periods of 3–9 yr. The cause of the high frequent ENSO is still unclear, but our model result corroborates previous suggestions that the horizontal resolution of the atmospheric model plays a dominant role (Guilyardi et al., 2004) as well as the Walker circulation (Guilyardi et al., 2003) and noise levels (Latif et al., 2001).

The ECHO-G CTL shows reasonable skill in simulating ENSO structures such as the tropical Pacific SST climate and its seasonal cycle, the warm pool and cold tongue, a single ITCZ pattern in the tropical eastern Pacific, the ENSO phase-locking to the annual cycle, and the ocean subsurface behaviour, such as eastward equatorial Kelvin and westward off-equatorial Rossby waves. However, the simulated strengths of SST variability in the eastern equatorial Pacific and the phase-locking to the annual cycle are larger than observed, and the westward propagation of zonal wind stress in the equatorial Pacific cannot be reproduced by the model. Atmospheric responses to the ENSO, which are analysed by correlation and regression maps with both NINO3 and SOI indices, are also simulated realistically by ECHO-G. The model belongs to the Group I category defined by AchutaRao and Sperber (2002), which comprises the AOGCMs with best skill in reproducing atmospheric responses to the ENSO: the positive phase of the ENSO, i.e. El Niño, is associated with a well-structured weakening of the Walker circulation, an enhanced warming extending from the tropical central Pacific to the west coast of South America, and an associated rainfall in the tropical Pacific. It is found that the ECHO-G model is additionally able to reproduce a warming over northern North America during warm events.

A near white noise spectrum of the detrended NAO index is obtained for the observations and the model simulation. The observed atmospheric patterns associated with the NAO are compared with the simulated patterns. The quadrupole T2m structure over the Atlantic sector, wet and dry conditions over northern and southern Europe, respectively, and the dominant dipole structure of the MSLP over the Atlantic are well reproduced by the ECHO-G CTL. While the observed MSLP has little correlation with the NAO index over the Pacific sector, the modelled MSLP reveals significant positive correlations over the North Pacific. This is a common problem found in many AOGCMs, which might be caused by a too strong Atlantic–Pacific teleconnection (Stephenson and Pavan, 2003).

A simple trend analysis shows that the observed positive trend of the NAO index in the recent 40–60 yr cannot be found in the 1000-yr run, while the recent 10–30 yr trends are simulated with a chance of more than 1%. This is in accordance with previous work using HadCM2 and HadCM3 control runs (Osborn et al., 1999; Collins et al., 2001). However, the detection of the anthropogenic effect on the NAO is still incomprehensible because of model-dependent responses of the NAO to greenhouse gas warming and the signal-contaminated observations (e.g. SST).

6. Acknowledgments

The authors would like to thank Keith Rodgers for preparing the thermocline data set, as well as two anonymous reviewers for their constructive comments. This research was performed for the project ‘Research on the Development of Regional Climatic Change Scenarios to Prepare the National Climate Change Report’ of the Korean Meteorological Research Institute and for the DFG (German Research Foundation) project He1916/8. The model was run on an NEC SX-4 at the DKRZ, Hamburg, Germany.

References

- AchutaRao, K. and Sperber, K. R. 2002. Simulation of the El Niño Southern Oscillation: results from the coupled model intercomparison project. *Climate Dyn.* **19**, 191–209.
- Allen, M. R., Stott, P. A., Mitchell, J. F. B., Schnur, R. and Thomas L. D. 2000. Quantifying the uncertainty in forecasts of anthropogenic climate change. *Nature* **407**, 617–620.
- Blanke, B., Neelin, J. D. and Gutzler, D. 1997. Estimating the effect of stochastic wind stress forcing on ENSO irregularity. *J. Climate* **10**, 1473–1486.
- Bretherton, C. S. and Battisti, D. S. 2000. An interpretation of the results from atmospheric general circulation models forced by the time history of the observed sea surface temperature distribution. *Geophys. Res. Lett.* **27**, 767–770.
- Chang, P., Wang, B., Li, T. and Ji, L. 1994. Interactions between the seasonal cycle and the southern oscillation – frequency entrainment and chaos in a coupled ocean–atmosphere model. *Geophys. Res. Lett.* **21**, 817–820.
- Collins, M., Tett, S. F. B. and Cooper, C. 2001. The internal climate variability of HadCM3, a version of the Hadley Centre coupled model without flux adjustments. *Climate Dyn.* **17**, 61–81.
- Davey, M. K., Huddleston, M., Sperber, K. R., Braconnot, P., Bryan, F. and co-authors. 2002. STOIC: a study of coupled model climatology and variability in tropical ocean regions. *Climate Dyn.* **18**, 403–420.
- Eckert, C. and Latif, M. 1997. Predictability of a stochastically forced hybrid coupled model of El Niño. *J. Climate* **10**, 1488–1504.
- Fedorov, A. and Philander, S. G. 2000. Is El-Niño changing? *Science* **288**, 1997–2002.
- Frey, H., Latif, M. and Stockdale, T. 1997. The coupled GCM ECHO-2. Part I: The tropical Pacific. *Mon. Wea. Rev.* **125**, 703–720.
- Fyfe, J. C., Boer, G. J. and Flato, G. M. 1999. The Arctic and Antarctic Oscillations and their projected changes under global warming. *Geophys. Res. Lett.* **26**, 1601–1604.
- Gillett, N. P., Allen, M. R. and Tett, S. F. B. 2000. Modelled and observed variability in atmospheric vertical temperature structure. *Climate Dyn.* **16**, 49–61.
- Glowienka-Hense, R. 1990. The North Atlantic Oscillation in the Atlantic-European SLP. *Tellus* **42A**, 497–507.
- Guilyardi, E., Delecluse, P., Gualdi, S. and Navarra, A. 2003. Mechanisms for ENSO phase change in a coupled GCM. *J. Climate* **16**, 1141–1158.
- Guilyardi, E., Gualdi, S., Slingo, J., Navarra, A., Delecluse, P. and co-authors. 2004. Representing El Niño in coupled ocean–atmosphere GCMs: the dominant role of the atmosphere component. *J. Climate* **17**, 4623–4629.
- Hoerling, M. P., Hurrell, J. W. and Xu, T. 2001. Tropical origins for recent North Atlantic climate change. *Science* **292**, 90–93.
- Holland, M. M. 2003. The North Atlantic Oscillation–Arctic Oscillation in the CCSM2 and its influence on Arctic climate variability. *J. Climate* **16**, 2767–2781.
- Hulme, M. 1992. A 1951–80 global land precipitation climatology for the evaluation of general circulation models. *Climate Dyn.* **7**, 57–72.
- Hurrell, J. M. 1995. Decadal trends in the North Atlantic Oscillation: regional temperatures and precipitation. *Science* **269**, 676–679.
- Hurrell, J. M. 1996. Influence of variations in extratropical wintertime teleconnections on Northern Hemisphere temperature. *Geophys. Res. Lett.* **23**, 665–668.
- Hurrell, J. W. and van Loon, H. 1997. Decadal variations in climate associated with the North Atlantic Oscillation. *Climate Change* **36**, 301–326.
- IPCC, 2001. *Climate Change 2001: The Scientific Basis. Contribution of Working Group I to the Third Assessment Report of the Intergovernmental Panel on Climate Change* (eds J. T. Houghton, Y. Ding, D. J. Griggs, M. Noguer, P. J. van der Linden et al.). Cambridge University Press, Cambridge, 881 pp.
- Jones, P. D. and Moberg, A. 2003. Hemispheric and large-scale surface air temperature variations: an extensive revision and an update to 2001. *J. Climate* **16**, 206–223.
- Jones, P. D., Jonsson, T. and Wheeler, D. 1997. Extension to the North Atlantic Oscillation using early instrumental pressure observations from Gibraltar and South-West Iceland. *Int. J. Climatol.* **17**, 1433–1450.
- Josey, S., Kent, E. and Taylor, P. 1999. New insights into the ocean heat budget closure problem from analysis of the SOC air–sea flux climatology. *J. Climate* **12**, 2856–2880.
- Kistler, R., Kalnay, E., Collins, W., Saha, S., White, G. and co-authors. 2001. The NCEP/NCAR 50-yr reanalysis: monthly means CD-ROM and documentation. *Bull. Am. Meteorol. Soc.* **82**, 247–267.
- Latif, M., Sperber, K., Arblaster, J., Braconnot, P., Chen, D. and co-authors. 2001. ENSIP: the El Niño simulation intercomparison project. *Climate Dyn.* **18**, 255–276.
- Mechoso, C. R., Robertson, A. W., Barth, N., Davey, M. K., Delecluse, P. and co-authors. 1995. The seasonal cycle over the tropical Pacific in coupled ocean–atmosphere general circulation models. *Mon. Wea. Rev.* **123**, 2825–2838.
- Min, S.-K., Legutke, S., Hense, A. and Kwon, W.-T. 2005. Internal variability in a 1000-yr control simulation with the coupled climate model ECHO-G – I. Near-surface temperature, precipitation and mean sea level pressure. *Tellus* **57A**, 605–621.
- Neelin, J. D., Battisti, D. S., Hirst, A. C., Jin, F. F., Wakata, Y. and co-authors. 1998. ENSO theory. *J. Geophys. Res.* **103**, 14 261–14 290.
- Osborn, T. J., Briffa, K. R., Tett, S. F. B., Jones, P. D. and Trigo, R. M. 1999. Evaluation of the North Atlantic Oscillation as simulated by a coupled climate model. *Climate Dyn.* **15**, 685–702.
- Paeth, H., Hense, A., Glowienka-Hense, R., Voss, R. and Cubasch, U. 1999. The North Atlantic Oscillation as an indicator for greenhouse-gas induced regional climate change. *Climate Dyn.* **15**, 953–960.
- Paeth, H., Latif, M. and Hense, A. 2003. Global SST influence on twentieth-century NAO variability. *Climate Dyn.* **21**, 63–75.

- Rayner, N. A., Horton, E. B., Parker, D. E., Folland, C. K. and Hackett, R. B. 1996. Version 2.2 of the global sea-ice and sea surface temperature data set, 1903–1994. *Hadley Centre Climate Research Technical Note*, CRTN 74, September, Hadley Centre, Meteorological Office, Bracknell, UK, 21 pp.
- Rayner, N. A., Parker, D. E., Horton, E. B., Folland, C. K., Alexander, L. V. and co-authors. 2003. Global analyses of SST, sea ice and night marine air temperature since the late nineteenth century. *J. Geophys. Res.* **108**(D14), 4407 (doi:10.1029/2002JD002670).
- Robertson, A. W., Mechoso, C. R. and Kim, Y. J. 2000. The influence of Atlantic sea surface temperature anomalies on the North Atlantic Oscillation. *J. Climate* **13**, 122–138.
- Rodgers, K. B., Friederichs, P. and Latif, M. 2004. Tropical Pacific decadal variability and its relation to decadal modulations of ENSO. *J. Climate* **17**, 3761–3774.
- Rodwell, M. J., Rowell, D. P. and Folland, C. K. 1999. Oceanic forcing of the wintertime North Atlantic Oscillation and European climate. *Nature* **398**, 320–323.
- Roeckner, E., Oberhuber, J. M., Bacher, A., Christoph, M. and Kirchner, I. 1996. ENSO variability and atmospheric response in a global coupled atmosphere–ocean GCM. *Climate Dyn.* **12**, 737–754.
- Rogers, J. C. 1984. The association between the North Atlantic Oscillation and the Southern Oscillation in the Northern Hemisphere. *Mon. Wea. Rev.* **112**, 1999–2015.
- Rogers, J. C. 1990. Patterns of low-frequency monthly sea level pressure variability (1899–1986) and associated wave cyclone frequencies. *J. Climate* **3**, 1364–1379.
- Ropelewski, C. F. and Halpert, M. S. 1987. Global and regional scale precipitation patterns associated with the El Niño/Southern Oscillation. *Mon. Wea. Rev.* **115**, 1606–1626.
- Ropelewski, C. F. and Jones, P. D. 1987. An extension of the Tahiti–Darwin Southern Oscillation Index. *Mon. Wea. Rev.* **115**, 2161–2165.
- Shindell, D. T., Miller, R. L., Schmidt, G. and Pandolfo, L. 1999. Simulation of the Arctic Oscillation trend by greenhouse forcing of a stratospheric model. *Nature* **399**, 452–455.
- Stephenson, D. B. and Pavan, V. 2003. The North Atlantic Oscillation in coupled climate models: a CMIP1 evaluation. *Climate Dyn.* **20**, 381–399.
- Stephenson, D. B., Pavan, V. and Bojariu, R. 2000. Is the North Atlantic Oscillation a random walk? *Int. J. Climatol.* **20**, 1–18.
- Stott, P. A. and Kettleborough, J. A. 2002. Origins and estimates of uncertainty in predictions of twenty-first century temperature rise. *Nature* **416**, 723–726.
- Suarez, M. J. and Schopf, P. S. 1988. A delayed action oscillator for ENSO. *J. Atmos. Sci.* **45**, 3283–3287.
- Thompson, D. W. J. and Wallace, J. M. 1998. The Arctic Oscillation signature in the wintertime geopotential height and temperature fields. *Geophys. Res. Lett.* **25**, 1297–1300.
- Thompson, D. W. J. and Wallace, J. M. 2000. Annular modes in the extratropical circulation. Part I: Month-to-month variability. *J. Climate* **13**, 1000–1016.
- Thompson, D. W. J. and Wallace, J. M. 2001. Regional climate impacts of the Northern Hemisphere Annular Mode. *Science* **293**, 85–89.
- Timmermann, A., Latif, A., Voss, R. and Grötzner, A. 1998. Northern Hemisphere interdecadal variability: a coupled air–sea mode. *J. Climate* **11**, 1906–1931.
- Trenberth, K. E. and Caron, J. M. 2000. The Southern Oscillation revisited: sea level pressures, surface temperatures, and precipitation. *J. Climate* **13**, 4358–4365.
- van Loon, H. and Madden, R. A. 1981. The Southern Oscillation. Part I: Global associations with pressure and temperature in northern winter. *Mon. Wea. Rev.* **109**, 1150–1162.
- Venzke, S., Latif, M. and Villwock, A. 2000. The coupled GCM ECHO-2. Part II: Indian Ocean response to ENSO. *J. Climate* **13**, 1371–1383.
- White, W. B., Tourre, Y. and Kushnir, Y. 1999. Evolution of interdecadal variability in sea level pressure, sea surface temperature, and upper ocean temperature over the Pacific Ocean. *J. Phys. Oceanogr.* **29**, 1528–1541.
- Wunsch, C. 1999. The interpretation of short climate records, with comments on the North Atlantic and Southern Oscillations. *Bull. Am. Meteorol. Soc.* **80**, 245–256.
- Xie, P. and Arkin, P. A. 1997. Global precipitation: A 17-yr monthly analysis based on gauge observations, satellite estimates, and numerical model outputs. *Bull. Am. Meteorol. Soc.* **78**, 2539–2558.